nature geoscience

Article

https://doi.org/10.1038/s41561-023-01362-5

Titanium-rich basaltic melts on the Moon modulated by reactive flow processes

Received: 27 April 2023

Accepted: 14 December 2023

Published online: 15 January 2024

Check for updates

Martijn Klaver[1,2] ✉, Stephan Klemme[1], Xiao-Ning Liu[2], Remco C. Hin[2,3,4], Christopher D. Coath[2], Mahesh Anand[5], C. Johan Lissenberg[6], Jasper Berndt[1] & Tim Elliott[2]

The origin of titanium-rich basaltic magmatism on the Moon remains enigmatic. Ilmenite-bearing cumulates in the lunar mantle are often credited as the source, but their partial melts are not a compositional match and are too dense to enable eruption. Here we use petrological reaction experiments to show that partial melts of ilmenite-bearing cumulates react with olivine and orthopyroxene in the lunar mantle, shifting the melt composition to that of the high-Ti suite. New high-precision Mg isotope data confirm that high-Ti basalts have variable and isotopically light Mg isotope compositions that are inconsistent with equilibrium partial melting. We employ a diffusion model to demonstrate that kinetic isotope fractionation during reactive flow of partial melts derived from ilmenite-bearing cumulates can explain these anomalously light Mg isotope compositions, as well as the isotope composition of other elements such as Fe, Ca and Ti. Although this model does not fully replicate lunar melt–solid interaction, we suggest that titanium-rich magmas erupted on the surface of the Moon can be derived through partial melting of ilmenite-bearing cumulates, but melts undergo extensive modification of their elemental and isotopic composition through reactive flow in the lunar mantle. Reactive flow may therefore be the critical process that decreases melt density and allows high-Ti melts to erupt on the lunar surface.

The Moon has a protracted history of basaltic volcanism at its surface, with activity continuing at least until 2.0 billion years ago[1,2]. Lunar basalts returned by NASA's Apollo missions display a much greater compositional diversity than their terrestrial counterparts. Most prominent is the two-orders-of-magnitude variation in Ti contents of primitive basaltic glasses, reaching exceptionally high concentrations of 18 wt% TiO_2 in the so-called high-Ti suite[3,4]. Notable Ti enrichment of their sources is required to produce such high-Ti basaltic melts, which is often linked to ilmenite-rich cumulate reservoirs that might be present in the lunar mantle.

Within the lunar magma ocean (LMO) paradigm[5,6], the interior of the Moon is shaped by the progressive crystallization of a global magma ocean[7] that, upon solidification, produced a stratified cumulate mantle dominated by olivine- and orthopyroxene-rich lithologies (harzburgites, dunites) and a flotation cumulate anorthosite crust[8,9]. After ~95% solidification of the LMO, saturation of the residual melt with Fe–Ti oxides caused the precipitation of ilmenite-bearing cumulates (IBC) directly below the anorthosite crust. The gravitational instability created by high-density IBC overlying less dense harzburgite probably led to overturning of the lunar cumulate pile whereby IBC were

---

[1]Institut für Mineralogie, Universität Münster, Münster, Germany. [2]School of Earth Sciences, University of Bristol, Bristol, UK. [3]Bayerisches Geoinstitut, Universität Bayreuth, Bayreuth, Germany. [4]Institute of Environmental Geology and Geoengineering, Consiglio Nazionale delle Ricerche (CNR), Milan, Italy. [5]School of Physical Sciences, The Open University, Milton Keynes, UK. [6]School of Earth and Environmental Sciences, Cardiff University, Cardiff, UK. ✉e-mail: klaverm@uni-muenster.de

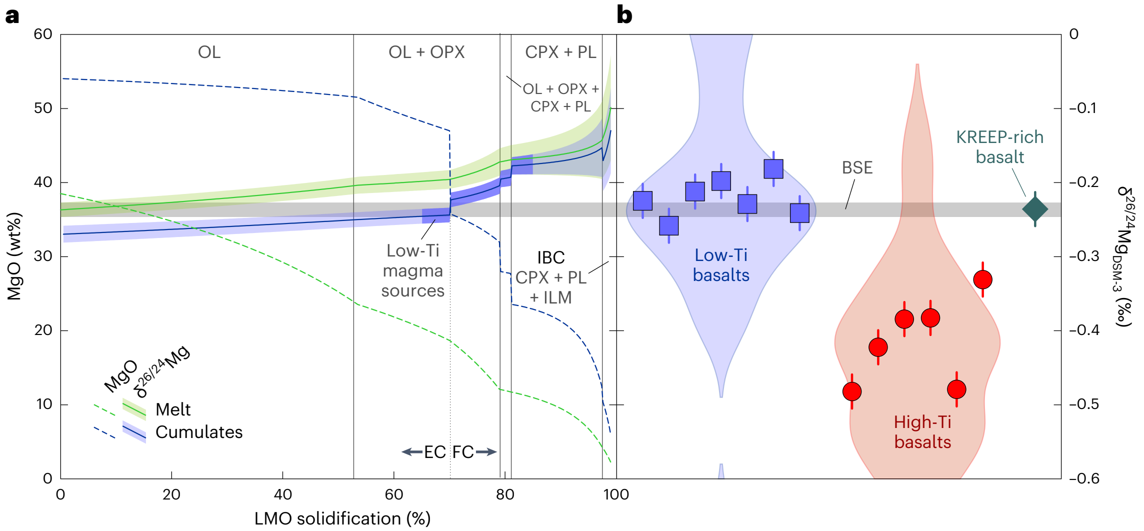

Fig. 1 | Magnesium isotope systematics of the Moon. a, Model of the evolution of $\delta^{26/24}$Mg (solid lines; right ordinate) and MgO content (dashed lines; left ordinate) in the residual melt and instantaneous cumulates during crystallization of the lunar magma ocean. The models show the mean with a 2 s uncertainty band for $\delta^{26/24}$Mg that incorporates the uncertainty on the olivine–melt Mg isotope fractionation factor and that on $\delta^{26/24}$Mg of the bulk Moon, which we take to be that of the bulk silicate Earth (BSE)[30,34] (Methods). The horizontal grey bar is the BSE composition that is taken as the starting point of the model. The instantaneous cumulate phases comprise olivine (OL), orthopyroxene (OPX), clinopyroxene (CPX), ilmenite (ILM) and 7 wt% plagioclase (PL) when present (remaining plagioclase is assumed to float to form the lunar anorthosite crust). Crystallizing phase assemblages are shown at the top; IBC crystallize from the last 2.5% melt. The model is based on equilibrium crystallization (EC) up to 70% LMO solidification with fractional crystallization (FC) of the remaining melt. The composition of cumulates that are a likely source for low-Ti magmas is shown in a darker shade of blue at 65–85% LMO solidification. **b**, Magnesium isotope composition ($\delta^{26/24}$Mg) of lunar basalts, grouped into low-Ti basalts (<4.5 wt% TiO_2), high-Ti basalts (8.5–13.5 wt% TiO_2) and a basalt rich in a K, rare-earth elements and P (KREEP) component (2 wt% TiO_2). Uncertainties are 2 s based on the pooled 2 s.d. of 13 reference material measurements (Supplementary Fig. 1). The shaded fields are kernel density diagrams of previous Mg isotope data for lunar basalts[27–29].

---

transported, at least in part, down towards the core as negatively buoyant diapirs[10–12]. Partial melting of fusible, Ti-rich IBC fragments in the lunar mantle is an attractive explanation for the generation of high-Ti basaltic melts[13,14], but one fraught with inconsistencies. Central to this debate is the sharp contrast in composition between IBC partial melts as inferred from experimental studies[15,16] and high-Ti basalts. Although trace element patterns of high-Ti samples support their derivation from IBC[8,17,18], major element systematics do not agree. Partial melts of IBC are ferroan and saturated in clinopyroxene, whereas the natural high-Ti basalts are magnesian and multiply saturated with olivine and orthopyroxene[19,20]. Furthermore, IBC partial melts have a higher density than ambient harzburgite and might therefore be unable to erupt at the surface of the Moon[21].

We propose a scenario that can unify these disparate observations, in which high-Ti basalts originate as IBC partial melts but have their composition modified through reaction with ambient harzburgite cumulates. Magnesium isotope compositions are a sensitive tracer of Fe–Mg exchange during mineral–melt reactions[22–24] and are therefore well suited to test this hypothesis. We combine high-precision Mg isotope ratio measurements of lunar basalts with high-temperature reaction experiments to argue that the composition of lunar high-Ti melts is shaped by reactive flow in the lunar mantle.

Magnesium isotope systematics of the Moon

Progressive solidification of a global LMO produces a range of cumulate lithologies with subtly different $\delta^{26/24}$Mg (the deviation in ^{26}Mg/^{24}Mg relative to the DSM-3 reference material). We modelled the Mg isotope evolution during crystallization of the LMO (Fig. 1a and Methods) to interpret the Mg isotope composition of lunar basalts. Recent quantification of the olivine–melt Mg isotope fractionation factor[25], when combined with ab initio constraints on inter-mineral Mg isotope fractionation[26], allows for more robust calculation of the $\delta^{26/24}$Mg of crystallizing phases (cumulates) and residual melt than done previously[27].

Olivine and orthopyroxene are the crystallizing phases up to ~80% solidification of the LMO, followed by plagioclase, clinopyroxene and ultimately ilmenite[8,9]. Both olivine and orthopyroxene have a slight affinity for the lighter isotopes of Mg relative to melt[25,26], and their crystallization drives the residual melt to higher $\delta^{26/24}$Mg (Fig. 1a). Subsequent crystallization of clinopyroxene causes a further modest increase in $\delta^{26/24}$Mg of the residual melt to about −0.14‰ after 98% LMO solidification. The complementary cumulate lithologies have $\delta^{26/24}$Mg between −0.27 and −0.15‰ (Fig. 1a).

The relatively limited Mg isotope variability calculated for the lunar cumulate mantle is in stark contrast with the heterogeneous $\delta^{26/24}$Mg of lunar basalts (Fig. 1). We present new, high-precision Mg isotope composition data for 14 Apollo programme lunar basalt samples that include seven low-Ti, low-K basalts, six high-Ti basalts and one low-Ti basalt with a high KREEP component (residual LMO melt rich in K, rare-earth elements and P). To achieve a higher precision than previous studies[27–29], we employed a critical mixture double spike technique (Methods) that explicitly corrects for instrumental mass fractionation without relying on identical behaviour of samples and reference materials during measurement[30,31]. This critical mixture double spike method allows interpretation of subtle differences in $\delta^{26/24}$Mg that cannot be resolved through conventional sample–standard bracketing and yields a 2 s precision of 0.023‰ on $\delta^{26/24}$Mg for the repeat measurement of reference materials (Supplementary Fig. 1).

Previous lower-precision data[27–29] showed high-Ti basalts to have on average lower $\delta^{26/24}$Mg than low-Ti basalts, and both suites to have comparable variance (Supplementary Fig. 3). Our new data show a similar bimodal distribution of $\delta^{26/24}$Mg as found previously, but by using the double spike technique and performing measurements on powders made from relatively large fragments of mare basalts (~250 mg), we demonstrate an important difference in variance of the low- and high-Ti suites. Low-Ti basalts have normally distributed $\delta^{26/24}$Mg of −0.22 ± 0.02‰ (2 s.e., $n = 7$). Harzburgite cumulates that

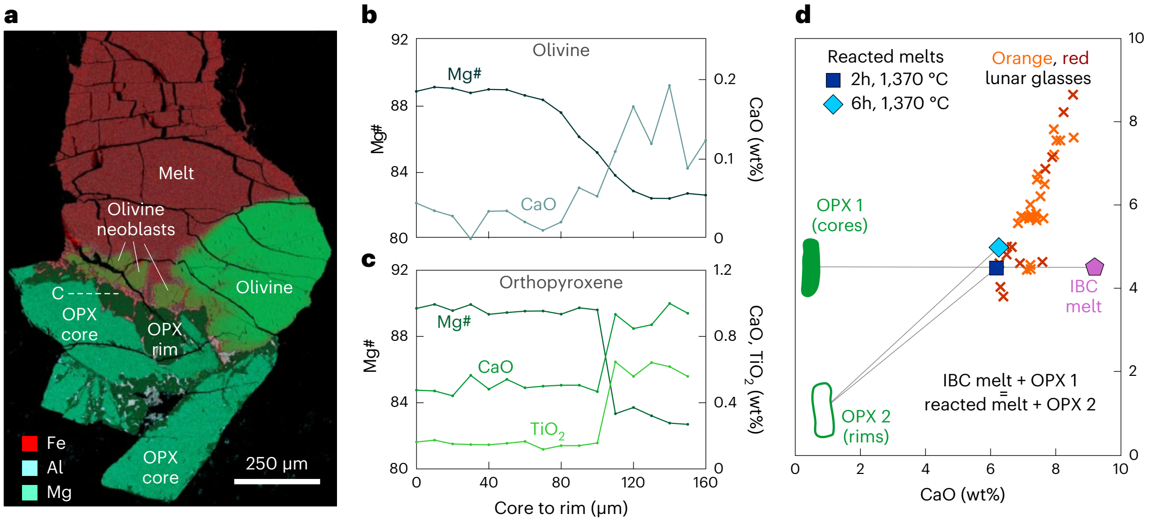

Fig. 2 | High-pressure reaction experiments of IBC partial melt with olivine and orthopyroxene. **a**, Mg–Fe–Al map of experiment GPC 823 (1,370 °C, 1.5 GPa, 2 h). Olivine undergoes coupled Fe–Mg exchange with the melt, seen as an undulate reaction front, thereby releasing Mg into the melt. Orthopyroxene shows strongly bimodal compositions with more Ca- and Ti-rich rims. The dashed line labelled 'C' is the orthopyroxene profile shown in panel **c**. **b**, Core-to-rim profiles of Mg# and CaO content through a representative olivine crystal (GPC 822 olivine 1; Supplementary Fig. 7). **c**, Core-to-rim profiles of Mg#, CaO and TiO$_2$ content through a representative orthopyroxene crystal (GPC 823; see dashed line in panel **a**). **d**, Diagram of CaO versus Al$_2$O$_3$ content illustrating the peritectic reaction between orthopyroxene and the IBC melt where the reactant orthopyroxene crystals have formed Ca-rich rims. The composition of orange and red primitive basaltic glasses[3,4] is shown for comparison.

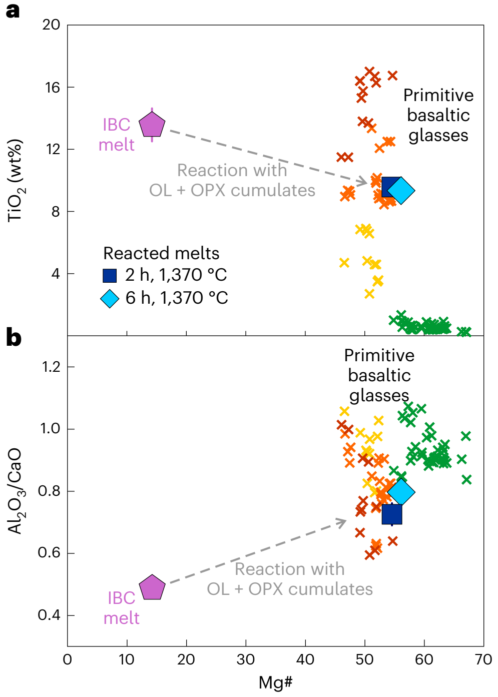

Fig. 3 | Reacted melt compositions. Composition of the IBC partial melt after reaction with olivine and orthopyroxene compared with primitive green, yellow, orange and red basaltic glasses from the Moon[3,4]. **a**, Mg# versus TiO$_2$ content. **b**, Mg# versus Al$_2$O$_3$/CaO.

precipitated at 65–85% LMO solidification are argued to be the main source of low-Ti basalts[18,32,33]. Low-degree partial melts of such a source have a modest Mg isotope fractionation of +0.03 to +0.05‰ relative to the bulk Moon (Supplementary Fig. 4). As a result, the homogeneous composition of the low-Ti basalts constrains the $\delta^{26/24}$Mg of the bulk Moon to be −0.26 ± 0.02‰, which is indistinguishable from the bulk silicate Earth composition (−0.24 ± 0.01‰ (refs. 30,34)).

Conversely, high-Ti basalts do not form a homogeneous population and have notably lower $\delta^{26/24}$Mg, ranging from −0.33 to −0.48‰ (Fig. 1b), which is at odds with equilibrium partial melting. The isotopically light composition of the high-Ti basalts cannot be tied directly to any cumulate reservoir. Our modelling shows that IBC, which have been argued to contribute to high-Ti magmatism, and partial melts thereof have a clearly heavier Mg isotope composition ($\delta^{26/24}$Mg = −0.14 ± 0.05‰) than high-Ti basalts. Hence, equilibrium Mg isotope fractionation during partial melting of IBC, or any lunar cumulate reservoir or hybrid source for that matter, cannot produce the low and variable $\delta^{26/24}$Mg of the high-Ti basalts. Moreover, preferential dissolution of ilmenite from IBC into low-Ti magmas at low pressure, which has also been proposed as a mechanism to form the high-Ti suite[20,35], is also inconsistent with the Mg isotope data. Ilmenite in late-stage cumulates contains very little Mg (ref. 9), and its preferential dissolution will therefore not have the capacity to drastically change $\delta^{26/24}$Mg of the Mg-rich low-Ti melts.

If the highly ferroan IBC partial melts (Mg# <25) (ref. 16) are parental to the high-Ti suite (Mg# >45) (refs. 3,4), they need to gain Mg to increase their Mg#. If Mg gain occurred without chemical equilibration, due to diffusive limitations, it would be accompanied by kinetic isotope fractionation. Their large relative mass differences make Mg isotopes highly amenable to kinetic fractionation[22–24]. As lighter isotopes diffuse faster than heavier isotopes, a net gain in Mg through diffusion into the lunar high-Ti melts can conceptually explain their enrichment in the lighter isotopes of Mg but raises questions about the specifics of how such a mechanism might operate.

The reaction between IBC partial melts and ambient mantle

Overturn of the lunar cumulate pile caused foundering of IBC as negative diapirs into the lunar mantle[10,11]. Experimental studies have shown that the solidus temperature of IBC is over 200 °C lower than that of harzburgite cumulates, and hence IBC will melt preferentially, forming partial melts with high Ti and Fe contents but low Mg# (refs. 15,16). The fate of IBC partial melts in the lunar mantle is uncertain[21]. Their composition is in strong chemical disequilibrium with the ambient lunar mantle, which consists of high-Mg# harzburgites. We experimentally

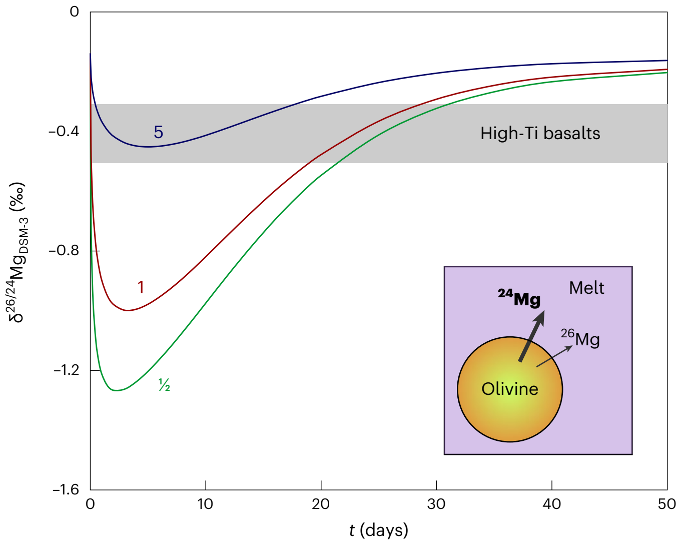

Fig. 4 | Magnesium isotope diffusion model. Change in $\delta^{26/24}$Mg of a finite mass of IBC partial melt upon diffusive Mg exchange with an olivine crystal, as shown schematically in the inset, for three melt–olivine ratios (curve labels). The grey-shaded field shows $\delta^{26/24}$Mg of the high-Ti lunar basalts. The diffusion modelling approach and parameters are provided in Methodsand Supplementary Table 5.

investigated the reaction between a synthetic IBC partial melt composition and primitive olivine (Mg# 89.1) and orthopyroxene (Mg# 89.6) crystals at a temperature (1,370 °C) and pressure (1.5 GPa) close to the multiple saturation point of high-Ti glasses[19] using a piston–cylinder press (Methods).

Olivine and orthopyroxene react vigorously with the IBC melt, resulting in notable changes in the composition of these phases (Fig. 2). Olivine undergoes coupled Fe–Mg exchange with the Fe-rich melt to attain Mg# equilibrium, leading to undulate diffusion fronts in the olivine crystals, but is otherwise stable in the IBC melt. The net result of this reaction is a diffusive release of Mg into the melt and incorporation of Fe into olivine, thereby increasing melt Mg#. Olivine rims and small, euhedral neoblasts (Fig. 2a) have attained Mg# equilibrium with the reacted melt ($D_{\mathrm{Fe-Mg}}$ = 0.30–0.33). Orthopyroxene displays a replacive texture with strongly bimodal compositions. Orthopyroxene rims have lower Mg# and notably higher CaO and TiO_2 contents compared with the cores (Fig. 2c).

The composition of the melt is strongly modified by the reaction with olivine and orthopyroxene, leading to a decrease in CaO and TiO_2 content and increase in Al_2O_3/CaO and Mg# (Fig. 3). The decrease in melt CaO content indicates that orthopyroxene rims form in a peritectic reaction where the original orthopyroxene crystals have partly dissolved to reprecipitate new Ca- and Ti-rich rims (Fig. 2d). A key observation is that no evidence was found for the crystallization of clinopyroxene or ilmenite from the IBC melt, consistent with the absence of these phases at the experimentally determined multiple saturation points of the lunar high-Ti suite[19,20].

We observe a consistent evolution of the reacted melt composition towards the lunar orange primitive basaltic glasses with ~10 wt% TiO_2 (Fig. 3), irrespective of experimental run duration (2–6 h). Hence, partial melts of the IBC bulk composition used here[16] can be parental to the orange glasses. We found that TiO_2/CaO of the melt is conserved during the reaction with olivine and orthopyroxene. A higher proportion of ilmenite to clinopyroxene in bulk IBC can generate partial melts with higher initial TiO_2 contents that can react with ambient harzburgites to form melts with a composition akin to the red glasses.

Reactive flow eases the problem that IBC partial melts have a higher density than the ambient mantle and, once formed, will segregate towards the core[21]. Molecular dynamics simulations indicate that high-Ti orange glass melts are positively buoyant with respect to a harzburgite mantle at any lunar pressure ($\rho < 3.3$ g cm^{-3}) (ref. 36). Hence, even if IBC partial melts are initially negatively buoyant, Fe–Mg exchange with the ambient harzburgite mantle and partial dissolution of orthopyroxene can decrease their density sufficiently to allow them to erupt on the surface.

Isotopic signatures of reactive melt flow

The reaction experiments demonstrate the direction of elemental transport when an IBC partial melt interacts with ambient harzburgite mantle. The IBC melt gains Mg through diffusion from olivine and partial dissolution of orthopyroxene and loses Fe, Ca and Ti to the peritectic orthopyroxene rims and, to a smaller extent, olivine (Fig. 2). A corollary of the elemental exchange between melt and crystals is that it can drive kinetic isotope fractionation that overprints the primary isotopic composition of the IBC melt. The faster diffusion of light isotopes means that olivine will release isotopically light Mg into the melt[23] and itself acquire elevated $\delta^{26/24}$Mg (refs. 24,37), which is consistent with the low $\delta^{26/24}$Mg of the high-Ti suite. Diffusion-driven kinetic Mg isotope fractionation resulting from melt–rock interaction has also been proposed as an explanation for the slightly lower $\delta^{26/24}$Mg of terrestrial mid-ocean ridge basalts relative to predicted equilibrium partial melts of mantle peridotite[34]. Compared with terrestrial basaltic magmas, however, highly ferroan IBC partial melts have a much greater potential for diffusive Mg exchange between melt and ambient harzburgite as they are in strong Mg# disequilibrium (Figs. 2 and 3), and thus a more pronounced kinetic Mg isotope effect is expected. We modelled the decrease in $\delta^{26/24}$Mg of a finite mass of IBC melt upon diffusive exchange with an olivine crystal (Fig. 4 and Methods). This simplistic model is not intended to replicate the full process of lunar melt–solid interaction but to provide a first-order illustration of the magnitude of possible isotopic fractionation. The maximum perturbation of $\delta^{26/24}$Mg in the melt is dictated by the contrast in Mg# and the melt–olivine ratio, but for all scenarios modelled here (melt/olivine = 0.5–5.0), a single diffusive exchange event can change melt $\delta^{26/24}$Mg to that appropriate for the high-Ti basalts.

Although Mg isotopes are particularly diagnostic, the isotopic effects of reactive flow might also be visible in the isotopic composition of other elements. Magnesium isotope compositions are negatively correlated with $\delta^{44/40}$Ca measured on the same samples[32] (Fig. 5a). Calcium is lost from the IBC melt through diffusion into olivine (Fig. 2b), but the peritectic orthopyroxene rims are its main sink. Rapid crystallization of these rims drives Ca incorporation from Ca-depleted boundary layers that have low $\delta^{44/40}$Ca due to the faster diffusion of lighter Ca isotopes in the melt towards the boundary layer[38]. The peritectic orthopyroxene rims therefore develop low $\delta^{44/40}$Ca, as observed in terrestrial melt-metasomatized peridotites[39,40], driving the reacted melt to higher $\delta^{44/40}$Ca. As such, the Mg–Ca isotope covariation provides support for a kinetic effect imparted by the reaction of IBC partial melts with ambient harzburgite cumulates. Moreover, Fe–Mg exchange between olivine and melt will be accompanied by kinetic Fe isotope fractionation, drawing isotopically light Fe from the melt[24,37,39] (Fig. 5d). The dichotomy between high-Ti basalts with heavy Fe isotope compositions and lighter low-Ti basalts[41–43] (Fig. 5b) therefore provides additional support for reactive flow of IBC partial melts. Likewise, kinetic fractionation of Ti isotopes during incorporation of Ti into the peritectic orthopyroxene rims can contribute to the more variable Ti isotope compositions of high-Ti basalts relative to the low-Ti basalts and the bulk Moon composition[44,45] (Fig. 5c).

Trace elements and radiogenic isotopes are much less affected by reactive flow than these isotopic systematics, which are sensitive to diffusion-driven kinetic fractionation. The trace element composition of the high-Ti suite is consistent with partial melting of IBC that contain a variable but small proportion (0.5–3.0%) of trace element-rich

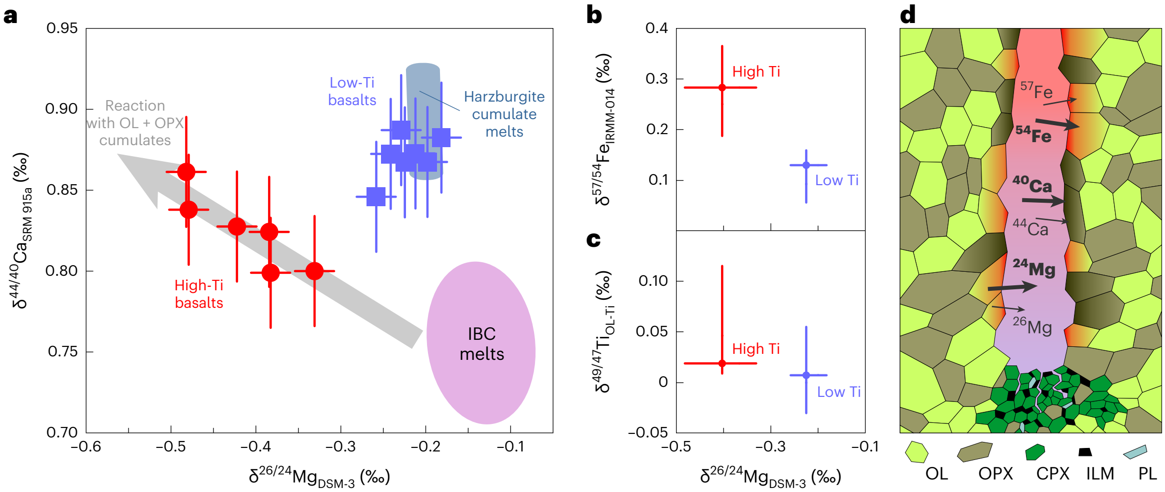

Fig. 5 | Diffusive exchange between IBC melt and ambient mantle. The reaction between the IBC melt and ambient olivine- and orthopyroxene-dominated cumulates drives diffusive elemental transport and kinetic isotope fractionation. **a**, Diagram displaying the covariation between $\delta^{26/24}$Mg and $\delta^{44/40}$Ca (relative to reference material SRM 915a) in lunar high-Ti basalts resulting from Ca loss to orthopyroxene and diffusion of Mg from olivine and orthopyroxene into the IBC melt. Low-Ti basalts display homogeneous Mg–Ca isotope compositions consistent with partial melting of orthopyroxene-rich cumulate source rocks. The IBC melts field represents low-degree partial melts of ilmenite-bearing cumulates[16] (Supplementary Fig. 5). For both partial melt fields, the Mg and Ca isotope compositions were calculated through an isotopic mass balance (Methods). Uncertainties for $\delta^{26/24}$Mg are 2 s based on the pooled 2 s.d. of 13 reference material measurements (Supplementary Fig. 1). Calcium isotope composition data and 2 s uncertainties for the samples are from ref. 32. **b**, Median and range for Mg (this study) and Fe isotope[41–43] compositions ($\delta^{57/54}$Fe relative to reference material IRMM-014) of low-Ti and high-Ti basalts. **c**, Median and range for Mg (this study) and Ti isotope[44,45] compositions ($\delta^{49/47}$Ti relative to reference material OL-Ti) of low-Ti and high-Ti basalts. **d**, The direction of elemental transport and kinetic isotope fractionation in the reaction between ambient olivine–orthopyroxene mantle and an IBC partial melt. The IBC melt composition is shifted to lower $\delta^{26/24}$Mg and higher Al$_2$O$_3$/CaO, Mg#, $\delta^{44/40}$Ca and $\delta^{57/54}$Fe.

trapped residual liquid[8,17,18]. As olivine and orthopyroxene both have low to very low partition coefficients for most trace elements, the reaction between the IBC partial melt and ambient harzburgite cumulates is unlikely to impose an effect that exceeds the variation generated during partial melting of the IBC. Hence, while trace elements systematics are related to subtle variations in IBC composition, the stable isotope composition of high-Ti basalts bears testament to reactive flow being the missing link between overturned IBC present in the lunar mantle and the high-Ti magmatic suite.

Online content

Any methods, additional references, Nature Portfolio reporting summaries, source data, extended data, supplementary information, acknowledgements, peer review information; details of author contributions and competing interests; and statements of data and code availability are available at https://doi.org/10.1038/s41561-023-01362-5.

References

1. Che, X. et al. Age and composition of young basalts on the Moon, measured from samples returned by Chang'e-5. *Science* **374**, 887–890 (2021).
2. Hiesinger, H., Jaumann, R., Neukum, G. & Head, J. W. III Ages of mare basalts on the lunar nearside. *J. Geophys. Res. Planets* **105**, 29239–29275 (2000).
3. Delano, J. W. Pristine lunar glasses: criteria, data, and implications. *J. Geophys. Res. Solid Earth* **91**, 201–213 (1986).
4. Shearer, C. & Papike, J. Basaltic magmatism on the Moon: a perspective from volcanic picritic glass beads. *Geochim. Cosmochim. Acta* **57**, 4785–4812 (1993).
5. Smith, J. V. et al. Petrologic history of the moon inferred from petrography, mineralogy and petrogenesis of Apollo 11 rocks. In *Proc. Apollo 11 Lunar Science Conference* 897–926 (1970).
6. Wood, J. A., Dickey, J. S. Jr, Marvin, U. B. & Powell, B. N. Lunar anorthosites and a geophysical model of the moon. In *Proc. Apollo 11 Lunar Science Conference* 965–988 (1970).
7. Lock, S. J. et al. The origin of the Moon within a terrestrial synestia. *J. Geophys. Res. Planets* **123**, 910–951 (2018).
8. Snyder, G. A., Taylor, L. A. & Neal, C. R. A chemical model for generating the sources of mare basalts: combined equilibrium and fractional crystallization of the lunar magmasphere. *Geochim. Cosmochim. Acta* **56**, 3809–3823 (1992).
9. Charlier, B., Grove, T. L., Namur, O. & Holtz, F. Crystallization of the lunar magma ocean and the primordial mantle–crust differentiation of the Moon. *Geochim. Cosmochim. Acta* **234**, 50–69 (2018).
10. Hess, P. C. & Parmentier, E. A model for the thermal and chemical evolution of the Moon's interior: implications for the onset of mare volcanism. *Earth Planet. Sci. Lett.* **134**, 501–514 (1995).
11. Zhao, Y., De Vries, J., van den Berg, A., Jacobs, M. & van Westrenen, W. The participation of ilmenite-bearing cumulates in lunar mantle overturn. *Earth Planet. Sci. Lett.* **511**, 1–11 (2019).
12. Zhang, N. et al. Lunar compositional asymmetry explained by mantle overturn following the South Pole–Aitken impact. *Nat. Geosci.* **15**, 37–41 (2022).
13. Ringwood, A. & Kesson, S. A dynamic model for mare basalt petrogenesis. In *Proc. Lunar and Planetary Science Conference* 1697–1722 (1976).
14. Su, B. et al. Fusible mantle cumulates trigger young mare volcanism on the Cooling Moon. *Sci. Adv.* **8**, eabn2103 (2022).
15. Mallik, A., Ejaz, T., Shcheka, S. & Garapic, G. A petrologic study on the effect of mantle overturn: Iimplications for evolution of the lunar interior. *Geochim. Cosmochim. Acta* **250**, 238–250 (2019).
16. van Orman, J. A. & Grove, T. L. Origin of lunar high-titanium ultramafic glasses: constraints from phase relations and dissolution kinetics of clinopyroxene–ilmenite cumulates. *Meteorit. Planet. Sci.* **35**, 783–794 (2000).
17. Hallis, L., Anand, M. & Strekopytov, S. Trace-element modelling of mare basalt parental melts: implications for a heterogeneous lunar mantle. *Geochim. Cosmochim. Acta* **134**, 289–316 (2014).

18. Beard, B. L., Taylor, L. A., Scherer, E. E., Johnson, C. M. & Snyder, G. A. The source region and melting mineralogy of high-titanium and low-titanium lunar basalts deduced from Lu–Hf isotope data. *Geochim. Cosmochim. Acta* **62**, 525–544 (1998).
19. Krawczynski, M. J. & Grove, T. L. Experimental investigation of the influence of oxygen fugacity on the source depths for high titanium lunar ultramafic magmas. *Geochim. Cosmochim. Acta* **79**, 1–19 (2012).
20. Wagner, T. & Grove, T. Experimental constraints on the origin of lunar high-Ti ultramafic glasses. *Geochim. Cosmochim. Acta* **61**, 1315–1327 (1997).
21. Tanton, L. T. E., van Orman, J. A., Hager, B. H. & Grove, T. L. Re-examination of the lunar magma ocean cumulate overturn hypothesis: melting or mixing is required. *Earth Planet. Sci. Lett.* **196**, 239–249 (2002).
22. Pogge von Strandmann, P. A. et al. Variations of Li and Mg isotope ratios in bulk chondrites and mantle xenoliths. *Geochim. Cosmochim. Acta* **75**, 5247–5268 (2011).
23. Richter, F. M., Watson, E. B., Mendybaev, R. A., Teng, F.-Z. & Janney, P. E. Magnesium isotope fractionation in silicate melts by chemical and thermal diffusion. *Geochim. Cosmochim. Acta* **72**, 206–220 (2008).
24. Teng, F.-Z., Dauphas, N., Helz, R. T., Gao, S. & Huang, S. Diffusion-driven magnesium and iron isotope fractionation in Hawaiian olivine. *Earth Planet. Sci. Lett.* **308**, 317–324 (2011).
25. Liu, X.-N. et al. Equilibrium olivine–melt Mg isotopic fractionation explains high δ^{26}Mg values in arc lavas. *Geochemical Perspect. Lett.* **22**, 42–47 (2022).
26. Schauble, E. A. First-principles estimates of equilibrium magnesium isotope fractionation in silicate, oxide, carbonate and hexaaquamagnesium (2+) crystals. *Geochim. Cosmochim. Acta* **75**, 844–869 (2011).
27. Sedaghatpour, F. & Jacobsen, S. B. Magnesium stable isotopes support the lunar magma ocean cumulate remelting model for mare basalts. *Proc. Natl Acad. Sci. USA* **116**, 73–78 (2019).
28. Sedaghatpour, F., Teng, F.-Z., Liu, Y., Sears, D. W. & Taylor, L. A. Magnesium isotopic composition of the Moon. *Geochim. Cosmochim. Acta* **120**, 1–16 (2013).
29. Wiechert, U. & Halliday, A. N. Non-chondritic magnesium and the origins of the inner terrestrial planets. *Earth Planet. Sci. Lett.* **256**, 360–371 (2007).
30. Hin, R. C. et al. Magnesium isotope evidence that accretional vapour loss shapes planetary compositions. *Nature* **549**, 511–515 (2017).
31. Coath, C. D., Elliott, T. & Hin, R. C. Double-spike inversion for three-isotope systems. *Chem. Geol.* **451**, 78–89 (2017).
32. Klaver, M. et al. The Ca isotope composition of mare basalts as a probe into the heterogeneous lunar mantle. *Earth Planet. Sci. Lett.* **570**, 117079 (2021).
33. Hess, P. C. On the source regions for mare picrite glasses. *J. Geophys. Res. Planets* **105**, 4347–4360 (2000).
34. Liu, X.-N. et al. The magnesium isotopic composition of the mantle. *Geochim. Cosmochim. Acta* **358**, 12–26 (2023).
35. van Kan Parker, M., Mason, P. R. & Van Westrenen, W. Trace element partitioning between ilmenite, armalcolite and anhydrous silicate melt: implications for the formation of lunar high-Ti mare basalts. *Geochim. Cosmochim. Acta* **75**, 4179–4193 (2011).
36. van Kan Parker, M. et al. Neutral buoyancy of titanium-rich melts in the deep lunar interior. *Nat. Geosci.* **5**, 186–189 (2012).
37. Sio, C. K. I. et al. Discerning crystal growth from diffusion profiles in zoned olivine by in situ Mg–Fe isotopic analyses. *Geochim. Cosmochim. Acta* **123**, 302–321 (2013).
38. Watson, E. B. & Müller, T. Non-equilibrium isotopic and elemental fractionation during diffusion-controlled crystal growth under static and dynamic conditions. *Chem. Geol.* **267**, 111–124 (2009).
39. Zhao, X. et al. Coupled extremely light Ca and Fe isotopes in peridotites. *Geochim. Cosmochim. Acta* **208**, 368–380 (2017).
40. Kang, J.-T. et al. Calcium isotopic fractionation in mantle peridotites by melting and metasomatism and Ca isotope composition of the Bulk Silicate Earth. *Earth Planet. Sci. Lett.* **474**, 128–137 (2017).
41. Liu, Y. et al. Oxygen and iron isotope constraints on near-surface fractionation effects and the composition of lunar mare basalt source regions. *Geochim. Cosmochim. Acta* **74**, 6249–6262 (2010).
42. Sossi, P. A. & Moynier, F. Chemical and isotopic kinship of iron in the Earth and Moon deduced from the lunar Mg-suite. *Earth Planet. Sci. Lett.* **471**, 125–135 (2017).
43. Poitrasson, F., Zambardi, T., Magna, T. & Neal, C. R. A reassessment of the iron isotope composition of the Moon and its implications for the accretion and differentiation of terrestrial planets. *Geochim. Cosmochim. Acta* **267**, 257–274 (2019).
44. Kommescher, S. et al. Unravelling lunar mantle source processes via the Ti isotope composition of lunar basalts. *Geochem. Perspect. Lett.* **13**, 13–18 (2020).
45. Millet, M.-A. et al. Titanium stable isotope investigation of magmatic processes on the Earth and Moon. *Earth Planet. Sci. Lett.* **449**, 197–205 (2016).

Publisher's note Springer Nature remains neutral with regard to jurisdictional claims in published maps and institutional affiliations.

Open Access This article is licensed under a Creative Commons Attribution 4.0 International License, which permits use, sharing, adaptation, distribution and reproduction in any medium or format, as long as you give appropriate credit to the original author(s) and the source, provide a link to the Creative Commons license, and indicate if changes were made. The images or other third party material in this article are included in the article's Creative Commons license, unless indicated otherwise in a credit line to the material. If material is not included in the article's Creative Commons license and your intended use is not permitted by statutory regulation or exceeds the permitted use, you will need to obtain permission directly from the copyright holder. To view a copy of this license, visit http://creativecommons.org/licenses/by/4.0/.

© The Author(s) 2024

Methods

Magnesium isotope composition measurements

The Mg isotope composition measurements were performed at the Bristol Isotope Group (University of Bristol) on homogeneous powders made out of ~250 mg fragments of lunar mare basalt samples recovered by the Apollo space programme. Aliquots of these powdered samples, which have previously been characterized for their major and trace element compositions[17], were digested in concentrated HF and HNO_3 (3/1) and subsequently treated twice with concentrated HNO_3. Upon complete dissolution, aliquots corresponding to 15–25 µg Mg were taken for Mg isotope composition measurements. Calcium isotope compositions ($\delta^{44/40}Ca_{SRM\,915a}$) have been determined on the same sample dissolutions[32]. Magnesium purification followed a double-pass protocol in 1.00 ± 0.02 M HNO_3 on cationic AG50w-X12 resin that is described in detail elsewhere[25]. Yields were checked by collecting 'splits' before and after Mg elution and were found to be ≥99.9%. The purified Mg fractions were dissolved in 0.3 M HNO_3 for measurement on a Thermo-Finnigan Neptune multi-collector inductively coupled plasma mass spectrometer (s/n 1020) using an Apex HF sample introduction system and Ni Jet+H cones. The Neptune was operated in medium-resolution mode (m/Δm > 6,000; 5–95% peak height definition) to resolve isobaric interferences such as $^{12}C^{14}N^+$ on $^{26}Mg^+$.

The purified Mg fractions were equilibrated with a ^{25}Mg–^{26}Mg double spike in an exact molar spike proportion, the 'critical mixture' (0.5908 for the Bristol Isotope Group Mg double spike[30]), which often required one to three iterations to achieve to within 0.15%. At this sample-to-spike ratio, the exponential-law instrumental mass fractionation parameter (β) and sample–spike mixing parameter (λ) degenerate into a single compound variable, thus reducing the number of independent isotope ratios required to solve the double spike equations from three to two[31]. As a result, the double spike technique[46] can be applied to Mg even though only three isotopes are available for measurement (^{24}Mg, ^{25}Mg and ^{26}Mg) (refs. 30,31). This method offers accurate correction for instrumental mass fractionation during measurement without relying on identical behaviour of samples and reference materials during measurement. The measurement strategies and data reduction adopted in this study are identical to those described in detail elsewhere[25,30,31] and discussed further in the Supplementary Discussion section 1.1.

The Mg isotope composition data are reported in the conventional delta notation[47] as $\delta^{26/24}Mg$ relative to the DSM-3 Mg reference material. Measurement precision for the lunar samples is ~0.011–0.013‰ (2 s.e.m.; Supplementary Table 1), but the pooled intermediate precision of reference materials BHVO-2 (basalt), JP-1 (peridotite) and DSM-3 (passed through the Mg purification procedure) of 0.023‰ (2 s, $n = 13$; Supplementary Fig. 1) is a better reflection of the true uncertainty of the method, and this value is shown as error bars in Figs. 1 and 4. Very similar 2 s intermediate precision of 0.027‰ (ref. 25) and 0.03‰ (ref. 48) was reported in other studies employing a critical mixture double spike technique, and our data for BHVO-2 and JP-1 agree very well with the results reported in these studies[25,30,48] (Supplementary Fig. 1 and Supplementary Table 3).

High-temperature reaction experiments

As a starting composition for the reaction experiments, we synthesized an ilmenite-bearing cumulate partial melt composition (TiCum12) that is based on the experimental study of ref. 16. This composition represents a comparatively low-degree partial melt ($F_{melt} = 0.53$) formed at 1,240 °C and 1.3 GPa that is saturated with ilmenite and clinopyroxene. The melt composition is highly ferroan (Mg# 15.3) and Ti rich (13.7 wt% TiO_2)[16]. The starting material was made by mixing high-purity oxides and carbonates under acetone followed by decarbonation for 2.5 h at 1,000 °C and re-homogenizing under acetone. The starting material was subsequently dried at 110 °C and kept dry for the experiments. An aliquot of the powdered starting material was placed in a small graphite capsule (volume ~2 mm^3) together with 3–5 fragments (~200–400 µm size fraction) of primitive, fresh olivine (Fo89.1) and orthopyroxene (Mg# 89.6) derived from a terrestrial fertile peridotite (spinel peridotite xenolith Vi314-58 from the Vitim volcanic field[49]). The proportion of IBC melt to minerals was aimed at 1:1:1. The graphite capsule containing the synthetic IBC partial melt, olivine and orthopyroxene was inserted into a Pt sleeve that was welded shut using a Lampert arc welder. The capsule was then placed in a piston–cylinder assembly consisting of crushable alumina, a graphite heater, Duran glass (Schott GmbH) and natural talc[50].

The reaction experiments were performed at the Institute for Mineralogy (University of Münster) using an end-loaded piston–cylinder apparatus[51] at a pressure of 1.5 GPa. A friction correction of −13% was applied on the basis of a calibration against the quartz–coesite transition[52] and the $MgCr_2O_4 + SiO_2 = MgSiO_3 + Cr_2O_3$ reaction[53], yielding a pressure that is accurate to within 0.07 GPa. Temperature was monitored and controlled using a W-Re thermocouple (type D) and a Eurotherm temperature controller. Several experiments were performed at 1,370–1,500 °C for run times ranging from 30 min to 6 h (Supplementary Table 6). The experiments were quenched by shutting off the power to the graphite heater before reducing the pressure. The experimental charges were mounted in epoxy, polished with a series of diamond pastes and measured for major element composition using the JEOL JXA 8530 F hyperprobe in Münster. Measurements were made using an acceleration voltage of 15 kV, a beam current of 15 nA and a spot size of 3 µm for silicate minerals and 20 µm for glasses. Of the five experiments performed in total, two were deemed successful and are reported here (GPC 822 and 823; Supplementary Table 6). In two rejected experiments, the melt came into contact with the noble metal capsule, leading to Fe loss and hence erroneous Mg# of the melt, but otherwise the reaction between IBC partial melt and olivine–orthopyroxene was identical. Another rejected experiment run at ~1,500 °C saw the complete dissolution of orthopyroxene. See Supplementary Discussion section 2 for more details. The two successful experiments conducted at 1,370 °C (2 and 6 h) showed substantial interaction between IBC melt and the olivine and orthopyroxene seeds and no evidence for contact between the IBC melt and the Pt outer capsule. A major element map for experiment GPC 823 (1,370 °C, 1.5 GPa, 2 h) was subsequently made at Cardiff University with a Zeiss Sigma FEG-SEM using dual 150 mm^2 energy-dispersive X-ray detectors.

Equilibrium Mg isotope fractionation modelling

The Mg isotope model of LMO crystallization is based on the 'EC model' reported by ref. 32 for Ca isotopes, and all pertinent details are listed therein. Briefly, the basis is a forward LMO crystallization model following an experimentally determined[9] crystallization sequence, phase proportions and phase compositions for a Lunar Primitive Upper Mantle[54] composition. This crystallization model gives the major element composition of the residual melt and instantaneous cumulate phases at each 0.5 wt% (up to 60 wt% solidification) or 0.2 wt% (>60 wt% solidification) crystallization step. As plagioclase predominantly floats to the surface to form the anorthosite crust, we introduce the concept of instantaneous sinking cumulates, which represent the plagioclase-poor assemblage that sinks to form the stratified lunar cumulate mantle. We consider that 7% plagioclase is trapped in these instantaneous sinking cumulates[8,16].

The Mg isotope composition of the residual melt and instantaneous sinking cumulates is subsequently calculated through isotopic mass balance. We employ the empirical olivine–melt Mg isotope fractionation factor determined by ref. 25 on equilibrated natural olivine–melt pairs ($\Delta^{26/24}Mg_{OL-melt} = -0.146 \pm 0.026‰ \times 10^6/T^2$), which is the only empirical, quantitative constraint available to date. We combine this olivine–melt Mg isotope fractionation factor with inter-mineral Mg isotope fractionation factors constrained through ab initio modelling[26] (Supplementary Table 4) to determine the temperature-dependent bulk Mg isotope fractionation factor at each crystallization step.

There are no ab initio Mg isotope fractionation factors for ilmenite, which appears late in the crystallization sequence (>97.5% LMO solidification) and then hosts only a minor fraction of Mg present in the instantaneous cumulates (<10%). We rely on natural data for ilmenite–olivine pairs that are in apparent equilibrium[55,56] and yield $\Delta^{26/24}\mathrm{Mg}_{\mathrm{ILM-OL}} = -0.353‰ \times 10^6/T^2$. The Mg budget hosted in plagioclase is negligible, and we arbitrarily set $\Delta^{26/24}\mathrm{Mg}_{\mathrm{PL-melt}}$ to zero. Taken together, the reduced partition function ratios, or β factors, for Mg are $\beta_{\mathrm{melt}} \geq \beta_{\mathrm{CPX}} > \beta_{\mathrm{OPX}} > \beta_{\mathrm{OL}} > \beta_{\mathrm{ILM}}$. This indicates that all crystallizing phases preferentially take in lighter Mg isotopes compared with silicate melt and therefore drive a steady increase in $\delta^{26/24}$Mg of the residual melt during LMO crystallization (Fig. 1a), consistent with the patterns displayed by terrestrial differentiation suites[25].

Modelling of $\delta^{26/24}$Mg of partial melts derived from various cumulate reservoirs employs the same Mg isotope fractionation factors. The composition of harzburgite cumulate partial melts in Fig. 5a is based on pMELTS models of partial melting of relatively evolved (70–95% LMO solidification) orthopyroxene-rich cumulates with minor olivine and clinopyroxene[32] combined with the Mg isotope LMO crystallization model. Harzburgite partial melts are ~0.03–0.05‰ heavier than the bulk Moon, and their $\delta^{26/24}$Mg is relatively insensitive to the degree of melting (Supplementary Fig. 4). Partial melting of IBC (Supplementary Fig. 5) is based on experimentally determined melting reactions and phase compositions[15,16]. More details on the partial melting modelling are given by ref. 32.

Diffusion modelling

The diffusive release of isotopically light Mg into the melt is a predicted result of the reaction between IBC melt and ambient harzburgite. We modelled a simplified scenario where we calculate a single event of Mg loss from a spherical olivine crystal (radius 0.25 mm) exposed to a finite mass of IBC melt based on the observed core-to-rim decrease in Mg# from ~89 to ~82 (Fig. 2b). The total amount of substance lost from a sphere through diffusion is given by equation 6.20 in ref. 57:

$$\frac{M_t}{M_\infty} = 1 - \frac{6}{\pi^2}\sum_{n=1}^{\infty}\frac{1}{n^2}\exp\left(-Dn^2\pi^2 t/a^2\right)$$

where M_t is the mass of Mg lost at time t, M_∞ is the total mass of Mg lost after complete re-equilibration to Mg# 82, D is the diffusion coefficient of Mg in olivine, n is a positive integer and a is the radius of the spherical olivine crystal (all parameters used in the model shown in Fig. 4 are given in Supplementary Table 5). The amount of Mg lost from olivine was added to the amount of Mg present in a finite mass of melt for melt–olivine ratios of 0.5, 1 and 5 (Fig. 4). This was done individually for each Mg isotope (^{24}Mg, ^{25}Mg and ^{26}Mg) where the difference in diffusion coefficient for these isotopes is expressed as:

$$\frac{D_i}{D_j} = \left(\frac{m_j}{m_i}\right)^{\beta}$$

The subscripts i and j signify an isotope of Mg, m is the mass of that isotope, and β is an empirical kinetic parameter[23]. We adopt a conservative value of 0.05 for β_{Mg} (ref.23,24), although values up to 0.16 have been suggested for β_{Mg} in olivine[37,58]. Taking a higher value for β_{Mg} will increase the kinetic isotope effect shown in Fig. 4, meaning that the minimum $\delta^{26/24}$Mg of the melt becomes even lower.

Data availability

Data are available through Mendeley Data at https://doi.org/10.17632/p9fjkcxvs6.1

References

46. Rudge, J. F., Reynolds, B. C. & Bourdon, B. The double spike toolbox. *Chem. Geol.* **265**, 420–431 (2009).
47. Coplen, T. B. Guidelines and recommended terms for expression of stable-isotope-ratio and gas-ratio measurement results. *Rapid Commun. Mass Spectrom.* **25**, 2538–2560 (2011).
48. He, Y. et al. High-precision and high-accuracy magnesium isotope analysis on multiple-collector inductively coupled plasma mass spectrometry using a critical mixture double spike technique. *Solid Earth Sci.* **7**, 188–199 (2022).
49. Ionov, D. Chemical variations in peridotite xenoliths from Vitim, Siberia: inferences for REE and Hf behaviour in the garnet-facies upper mantle. *J. Petrol.* **45**, 343–367 (2004).
50. Gervasoni, F., Klemme, S., Rohrbach, A., Grützner, T. & Berndt, J. Experimental constraints on the stability of baddeleyite and zircon in carbonate- and silicate-carbonate melts. *Am. Mineral.* **102**, 860–866 (2017).
51. Boyd, F. & England, J. Apparatus for phase-equilibrium measurements at pressures up to 50 kilobars and temperatures up to 1750 °C. *J. Geophys. Res.* **65**, 741–748 (1960).
52. Bose, K. & Ganguly, J. Quartz–coesite transition revisited: reversed experimental determination at 500–1,200 C° and retrieved thermochemical properties. *Am. Mineral.* **80**, 231–238 (1995).
53. Klemme, S. & O'Neill, H. S. The reaction $MgCr_2O_4+SiO_2=Cr_2O_3+MgSiO_3$ and the free energy of formation of magnesiochromite ($MgCr_2O_4$). *Contrib. Mineral. Petrol.* **130**, 59–65 (1997).
54. Longhi, J. Petrogenesis of picritic mare magmas: constraints on the extent of early lunar differentiation. *Geochim. Cosmochim. Acta* **70**, 5919–5934 (2006).
55. Chen, L.-M. et al. Magnesium isotopic evidence for chemical disequilibrium among cumulus minerals in layered mafic intrusion. *Earth Planet. Sci. Lett.* **487**, 74–83 (2018).
56. Tian, H.-C. et al. Diffusion-driven extreme Mg and Fe isotope fractionation in Panzhihua ilmenite: implications for the origin of mafic intrusion. *Geochim. Cosmochim. Acta* **278**, 361–375 (2020).
57. Crank, J. *The Mathematics of Diffusion* (Oxford Univ. Press, 1975).
58. Oeser, M., Dohmen, R., Horn, I., Schuth, S. & Weyer, S. Processes and time scales of magmatic evolution as revealed by Fe–Mg chemical and isotopic zoning in natural olivines. *Geochim. Cosmochim. Acta* **154**, 130–150 (2015).

Acknowledgements

We thank M. Trogisch and B. Schmitte for their help preparing the experimental samples. D. Ionov kindly provided the mineral separates used in the experiments. This project was funded by the STFC through grant no. ST/M007715/1 to T.E. and a Humboldt postdoctoral research fellowship to M.K. R.C.H. acknowledges support from ERC Starting Grant 949417 – VapLoss. S.K. is funded by DFG-SFB TRR-170 (publication number 210). M.A. acknowledges support from STFC grants nos. ST/T000228/1 and ST/X001180/1.

Author contributions

M.K. and T.E. conceived the study. M.K. performed the measurements, experiments and modelling and wrote the manuscript with input from all authors. S.K. designed the experimental set-up. X.-N.L., R.C.H. and C.D.C. developed the critical mixture Mg isotope method. M.A. contributed the lunar samples. C.J.L. made the SEM maps of the experiments. J.B. developed the EPMA protocol and performed the measurements.

Funding

Open access funding provided by Westfälische Wilhelms-Universität Münster.

Competing interests

The authors declare no competing interests.

Additional information

Supplementary information The online version contains supplementary material available at https://doi.org/10.1038/s41561-023-01362-5.

Correspondence and requests for materials should be addressed to Martijn Klaver.

Peer review information *Nature Geoscience* thanks the anonymous reviewers for their contribution to the peer review of this work. Primary Handling Editor: Tamara Goldin, in collaboration with the *Nature Geoscience* team.

Reprints and permissions information is available at www.nature.com/reprints.